



The ALMA Spectroscopic Survey in the HUDF: A Search for [C II] Emitters at $6 \leq z \leq 8$

Bade D. Uzgil^{1,2}, Pascal A. Oesch^{3,4}, Fabian Walter^{2,5}, Manuel Aravena⁶, Leindert Boogaard⁷, Chris Carilli², Roberto Decarli⁸, Tanio Díaz-Santos^{6,9,10}, Yoshi Fudamoto³, Hanae Inami¹¹, Rychard Bouwens⁷, Paulo C. Cortes^{12,13}, Pierre Cox¹⁴, Emmanuele Daddi¹⁵, Jorge González-López^{6,16}, Ivo Labbé¹⁷, Gergő Popping¹⁸, Dominik Riechers^{19,20}, Mauro Stefanon⁷, Paul Van der Werf⁷, and Axel Weiss²¹

¹ California Institute of Technology, 1200 E. California Blvd, Pasadena, CA 91125, USA; badeu@astro.caltech.edu

² National Radio Astronomy Observatory, Pete V. Domenici Array Science Center, P.O. Box 0, Socorro, NM 87801, USA

³ Department of Astronomy, University of Geneva, Ch. des Maillettes 51, 1290 Versoix, Switzerland

⁴ International Associate, Cosmic Dawn Center (DAWN) at the Niels Bohr Institute, University of Copenhagen and DTU-Space, Technical University of Denmark, Copenhagen, Denmark

⁵ Max-Planck-Institut für Astronomie, Königstuhl 17, D-69117, Heidelberg, Germany

⁶ Núcleo de Astronomía de la Facultad de Ingeniería y Ciencias, Universidad Diego Portales, Av. Ejército Libertador 441, Santiago, Chile

⁷ Leiden Observatory, Leiden University, P.O. Box 9513, NL-2300 RA Leiden, The Netherlands

⁸ INAF-Osservatorio di Astrofisica e Scienza dello Spazio, via Gobetti 93/3, I-40129, Bologna, Italy

⁹ Institute of Astrophysics, Foundation for Research and Technology—Hellas (FORTH), Heraklion, GR-70013, Greece

¹⁰ Chinese Academy of Sciences South America Center for Astronomy (CASSACA), National Astronomical Observatories, CAS, Beijing 100101, People's Republic of China

¹¹ Hiroshima Astrophysical Science Center, Hiroshima University, 1-3-1 Kagamiyama, Higashi-Hiroshima, Hiroshima 739-8526, Japan

¹² Joint ALMA Observatory—ESO, Av. Alonso de Córdova, 3104, Santiago, Chile

¹³ National Radio Astronomy Observatory, 520 Edgemont Rd, Charlottesville, VA 22903, USA

¹⁴ Sorbonne Université, UPMC Université Paris 6 & CNRS, UMR 7095, Institut d'Astrophysique de Paris, 98b boulevard Arago, F-75014 Paris, France

¹⁵ Laboratoire AIM, CEA/DSM-CNRS-Université Paris, France

¹⁶ Las Campanas Observatory, Carnegie Institution of Washington, Casilla 601, La Serena, Chile

¹⁷ Centre for Astrophysics and Supercomputing, Swinburne University of Technology, Melbourne, VIC 3122, Australia

¹⁸ European Southern Observatory, Karl-Schwarzschild-Strasse 2, D-85748, Garching, Germany

¹⁹ Department of Astronomy, Cornell University, Space Sciences Building, Ithaca, NY 14853, USA

²⁰ Max-Planck-Institut für Astronomie, Königstuhl 17, D-69117 Heidelberg, Germany

²¹ Max-Planck-Institut für Radioastronomie, Auf dem Hügel 71, D-53121 Bonn, Germany

Received 2020 October 9; revised 2021 February 18; accepted 2021 February 20; published 2021 May 5

Abstract

The Atacama Large Millimeter/submillimeter Array (ALMA) Spectroscopic Survey in the Hubble Ultra Deep Field (ASPECS) Band 6 scan (212–272 GHz) covers potential [C II] emission in galaxies at $6 \leq z \leq 8$ throughout a 2.9 arcmin^2 area. By selecting on known Ly α emitters (LAEs) and photometric dropout galaxies in the field, we perform targeted searches down to a 5σ [C II] luminosity depth $L_{[\text{C II}]} \sim 2.0 \times 10^8 L_{\odot}$, corresponding roughly to star formation rates (SFRs) of $10\text{--}20 M_{\odot} \text{ yr}^{-1}$ when applying a locally calibrated conversion for star-forming galaxies, yielding zero detections. While the majority of galaxies in this sample are characterized by lower SFRs, the resulting upper limits on [C II] luminosity in these sources are consistent with the current literature sample of targeted ALMA observations of $z = 6\text{--}7$ LAEs and Lyman-break galaxies (LBGs), as well as the locally calibrated relations between $L_{[\text{C II}]}$ and SFR—with the exception of a single [C II]-deficient, UV-luminous LBG. We also perform a blind search for [C II]-bright galaxies that may have been missed by optical selections, resulting in an upper limit on the cumulative number density of [C II] sources with $L_{[\text{C II}]} > 2.0 \times 10^8 L_{\odot}$ (5σ) to be less than $1.8 \times 10^{-4} \text{ Mpc}^{-3}$ (90% confidence level). At this luminosity depth and volume coverage, we present an observed evolution of the [C II] luminosity function from $z = 6\text{--}8$ to $z \sim 0$ by comparing the ASPECS measurement to literature results at lower redshift.

Unified Astronomy Thesaurus concepts: High-redshift galaxies (734); Interstellar medium (847)

1. Introduction

Characterizing the properties of the interstellar medium (ISM; dust and gas) of the first generations of galaxies is one of the prime goals in observational astrophysics. Given the likely role of early galaxies in cosmic reionization—the last major phase transition of the universe, which was completed by $z \sim 6$ —understanding their physical properties is of particular importance (e.g., Dayal & Ferrara 2018). Evidence has emerged that the ISM conditions of pre-reionization galaxies were very different than in their descendants at later cosmic epochs. This includes strong rest-frame UV emission lines from ground-based spectra (e.g., C III]; Stark et al. 2015; Mainali et al. 2018) as well as optical lines with extreme equivalent width measured via Spitzer colors ([O III] $\lambda 5007 + \text{H}\beta$;

Labbé et al. 2013; De Barros et al. 2019). All these measurements point to hard ionization fields, dominated by young, low-metallicity stars—very different from galaxies at later times.

The sensitivity of the Atacama Large Millimeter/submillimeter Array (ALMA) now allows one to obtain more detailed insights into the chemical and physical properties of early galaxies at $z \geq 6$. In particular, measurements of the [C II] 158 μm line of the ISM provide unique constraints on the molecular gas properties and star formation rates (SFRs) of galaxies (e.g., Díaz-Santos et al. 2013; Herrera-Camus et al. 2015). [C II] is often the dominant cooling line of the ISM, coming primarily from photodissociation regions and the cold neutral medium of molecular clouds (e.g., Vallini et al. 2013). As such, the [C II] line probes the gas from which stars are

formed in normal galaxies (Carilli & Walter 2013; De Looze et al. 2014; Zanella et al. 2018).

[C II] lies in a favorable frequency window for $6 \leq z \leq 8$ galaxies (ALMA band 6). Even though a very large number of $z > 6$ galaxies have now been identified from deep Hubble Space Telescope (HST) imaging (e.g., Bouwens et al. 2015; Finkelstein et al. 2015), only a small number of the brightest galaxies have been spectroscopically confirmed via their Ly α emission lines (e.g., Oesch et al. 2015; Zitrin et al. 2015), due to a higher opacity of the intergalactic medium at $z > 6$ in the neutral era of the universe (e.g., Schenker et al. 2012; Treu et al. 2013; Pentericci et al. 2014). [C II] detections with ALMA therefore promised to be an efficient new avenue to spectroscopically confirm high-redshift galaxies with missing Ly α emission.

[C II] has now been detected in several non-quasar host galaxies at $z > 6$ (see, e.g., Maiolino et al. 2015; Willott et al. 2015; Hashimoto et al. 2019; Bakx et al. 2020). However, its luminosity was often not as high as expected from the local relation between SFR and $L_{\text{[C II]}}$ (De Looze et al. 2014; Herrera-Camus et al. 2015). While relatively luminous [C II] emission is still found at $z \sim 4.5\text{--}5.5$ (e.g., Capak et al. 2015; Schaerer et al. 2020), evidence is building for a deficit in $L_{\text{[C II]}}$ and an evolution of the SFR– $L_{\text{[C II]}}$ relationship at $z > 6$ in the epoch of reionization (see, e.g., Pentericci et al. 2016; Laporte et al. 2019; Matthee et al. 2019; Harikane et al. 2020). Theoretically, this can be well explained with lower metallicities expected in early galaxies (Vallini et al. 2013; Lagache et al. 2018; Popping et al. 2019), and high surface densities of star formation in starbursting galaxies (Ferrara et al. 2019). Recent observations and reanalyses of earlier ALMA data have now led to a different possible scenario: a significantly larger scatter in $L_{\text{[C II]}}$ at high redshift compared to the local SFR– $L_{\text{[C II]}}$ relation, instead of a [C II] deficit (see, e.g., Carniani et al. 2018; Matthee et al. 2019). Additionally, surface brightness dimming could affect the detectability of [C II] emission (Carniani et al. 2020). However, the current data sets are still limited in size, and furthermore most of the early galaxies that have been observed with ALMA were selected as Ly α emitters (LAEs) (such that they had a previously known redshift), which can lead to a bias toward young, metal-poor, dust-free systems (see, e.g., Smit et al. 2018).

The ALMA large program ALMA Spectroscopic Survey in the Hubble Ultra Deep Field (ASPECS) provides the first full frequency scan in band 6 of the Hubble Ultra Deep Field (HUDF; Aravena et al. 2019; Decarli et al. 2019; González-López et al. 2019). These observations enable the unbiased search for emission lines, both molecular (CO) and atomic ([C I]) (Decarli et al. 2020; Boogaard et al. 2020) and [C II] (this paper). The HUDF was chosen because it represents the deepest data set available across all wavelengths. By design, this field does not include very massive and highly star-forming systems (such as submillimeter galaxies or quasars), but traces the field galaxy population that is most representative at each cosmic epoch (L^* and sub- L^* galaxies). The HUDF has been particularly important in the discoveries of the most distant galaxies known, from early studies of the $z > 6$ galaxy population (e.g., Bouwens et al. 2010; McLure et al. 2010; Oesch et al. 2010) to consecutively higher redshifts (now extending to $z \sim 10\text{--}12$; e.g., Ellis et al. 2013; Oesch et al. 2013). The frequency setup of the ASPECS band 6 scan covers the redshifted [C II] emission line from $6 < z < 8$, ideally matched to some of the most distant galaxies known in the HUDF. In the pilot observations of ASPECS, a number of

potential [C II] line candidates were reported (Aravena et al. 2016). However, as discussed in detail below, none of these candidates could be confirmed (at 5σ) in the deeper and more uniform observations obtained through the ASPECS large program. This is in line with other recent [C II] detections and upper limits that have been reported in other sources in the meantime.

In this paper, we exploit these deeper data from the ASPECS large program (LP) over the HUDF to constrain the [C II] emission from galaxies at $z = 6\text{--}8$. In particular, we search for [C II] emission from previously identified LAEs and Lyman-break galaxies (LBGs) in this field, also exploiting recent, very deep MUSE spectra (Inami et al. 2017), and we perform an additional blind search. Doing this, we constrain the SFR– $L_{\text{[C II]}}$ relationship as well as the [C II] luminosity function in the epoch of reionization. This paper is structured as follows. In Section 2 we describe the observational data that were used. Section 3 presents the results of the [C II] emission line searches, before we discuss their implications in Section 4. We finish with conclusions in Section 5.

Throughout this paper we use a concordance cosmology with $\Omega_M = 0.3$, $\Omega_\Lambda = 0.7$, $h = 0.7$. Magnitudes are presented in the AB system (Oke & Gunn 1983), and we use a Chabrier initial mass function (IMF, Chabrier 2003).

2. Observations

2.1. ASPECS LP Band 6 Data

ASPECS Band 6 data are presented in detail in, e.g., Decarli et al. (2020) and González-López et al. (2020). In brief summary, observations were conducted from 2017 March–April to 2018 May–July, surveying a 4.2 arcmin^2 area (at 10% mosaic primary beam response) in the HUDF with 85 ALMA pointings and a total observing time of ~ 80 hr, including overheads. During observing, the 12 m array was in either compact configuration C40-1 or C40-2 to ensure that galaxies were mostly or entirely spatially unresolved. The survey scanned the full bandwidth of ALMA B6 in eight non-overlapping frequency setups, providing continuous wavelength coverage from observed frequencies $\nu_{\text{obs}} = 212\text{--}272$ GHz. At these frequencies, redshifted [C II] emission can, in principle, be observed from redshifts $z = 5.99\text{--}7.97$.

Throughout this work, we make use of two data products resulting from the ASPECS Band 6 survey. For extracting spectra, we use the naturally weighted raw, or “dirty,” image cube, after applying a primary beam (PB) correction. Continuum from bright 1 mm sources has been subtracted from this cube, as described in González-López et al. (2020). We mask out data below the half-power beamwidth (HPBW), where the mosaic primary beam response is less than 50%, working only within the central 2.9 arcmin^2 in the survey footprint. The synthesized beam in the image cube is $\sim 1''.6 \times 1''.1$ at band center $\nu_{\text{obs, cen}} = 242$ GHz, and the pixel scale is $0''.2$ per pixel. We have rebinned frequency channels by a factor of 8, so that the spectral resolution is 62.5 MHz ($\sim 77 \text{ km s}^{-1}$ at $\nu_{\text{obs, cen}}$). The resulting mean rms is $0.30 \text{ mJy beam}^{-1}$ per channel. To convert this flux density to an equivalent line luminosity, we assume spatially unresolved emission and adopt a fiducial line velocity width $v_{\text{FWHM}} = 200 \text{ km s}^{-1}$ —representative of observed line widths (FWHM) for [C II] emission in $z \sim 6\text{--}7$ LAEs (see Table C.1 in Matthee et al. 2019)—to calculate flux (in units of Jy km s^{-1}), then divide the measured rms by a scale factor $\sqrt{v_{\text{FWHM}}/v_{\text{chn}}}$ to account for the number of spectral channels with velocity

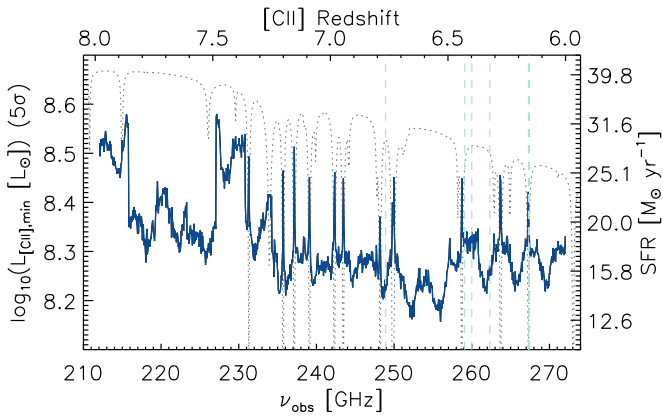


Figure 1. [C II] luminosity depth (5σ), assuming 200 km s^{-1} line width, across the survey bandwidth. The corresponding limit in SFR (right ordinate) is derived using a locally calibrated $L_{\text{[C II]}}-\text{SFR}$ relation for star-forming galaxies (De Looze et al. 2014). Dashed (light blue) vertical lines indicate the expected ν_{obs} for the [C II] line based on the $\text{Ly}\alpha$ redshift for the MUSE LAEs in the sample defined in Section 2.2: MUSE 852, 6332, 6312, 6524, 802, 560, in order of decreasing redshift. (Note that the vertical lines for MUSE 802 and 560 at the far right are nearly overlapping due to their proximity in redshift.) For illustrative purposes only, we have also plotted the atmospheric transmission (assuming precipitable water vapor (PWV) = 1 mm; dark gray, dotted curve) to show the effect of the atmospheric absorption features on the survey depth.

resolution ν_{chn} that span ν_{FWHM} .²² The 5σ line luminosity depth for the [C II] line as a function of observed frequency is shown in Figure 1, where the different features in the sensitivity arise due to a combination of integration time at different frequencies and atmospheric transmission (see also Decarli et al. 2020). For reference, imaging of the ASPECS Pilot data cube resulted in an average rms level of $0.42 \text{ mJy beam}^{-1}$ over the same channel width (Aravena et al. 2016). Combining the two data sets results in a marginal increase—by only a factor ~ 1.14 —in sensitivity over the relevant area of overlap between the LP and Pilot survey fields. We thus decided to proceed with the independent data sets.

Additionally, we use the 1.2 mm continuum map (without PB correction) with a mean rms of $9.3 \mu\text{Jy beam}^{-1}$ presented in González-López et al. (2020) to search for continuum emission in targeted optically selected galaxies (described in the following Section 2.2) and at positions returned by the blind search algorithm described in Section 3.2.

2.2. Ancillary Data Sets

To enable a targeted [C II] search in the ASPECS Band 6 data cube, we exploit existing galaxy catalogs in the HUDF with reliable photometric or spectroscopic redshifts.

Ly α emitters (LAEs)—The MUSE Hubble Ultra Deep Field Survey (Bacon et al. 2017) provides accurate spectroscopic redshifts for ~ 1500 galaxies in a 9 arcmin^2 field encompassing the full ASPECS footprint. With its wide instantaneous bandwidth, spanning $4650\text{--}9300 \text{ \AA}$, the MUSE IFU spectrometer provides continuous coverage of the $\text{Ly}\alpha$ emission line from $z=2.8\text{--}6.7$; we refer the interested reader to, e.g., Boogaard et al. (2019) for more information on observational details of the MUSE survey and complementarities with ASPECS. We consider sources located within the ASPECS

HPBW and which have secure spectroscopic redshifts within the ASPECS [C II] redshift coverage. These criteria yield six LAEs in our sample at $z=6.1\text{--}6.6$, drawn from the spectroscopic redshift catalog presented in Inami et al. (2017). The LAEs targeted here are characterized by $\text{Ly}\alpha$ fluxes $F_{\text{Ly}\alpha} = (1.5\text{--}11.2) \times 10^{-18} \text{ erg s}^{-1} \text{ cm}^{-2}$, corresponding to line luminosities $L_{\text{Ly}\alpha} = (0.66\text{--}1.5) \times 10^{42} \text{ erg s}^{-1}$, where $10^{42} \text{ erg s}^{-1}$ is approximately $0.2 L_{\text{Ly}\alpha}^*$ (Drake et al. 2017) at these redshifts. Their rest-frame $\text{Ly}\alpha$ equivalent widths (EWs) span a wide range, between ~ 7 and 140 \AA (T. Hashimoto 2021, private communication).

Lyman-break galaxies (LBGs)—We use the most comprehensive sample of $z > 6$ Lyman-break selected galaxies in the Extreme Deep Field (XDF) and GOODS-S fields that overlap with the ASPECS footprint, originally presented in Bouwens et al. (2015). Only sources within the ASPECS HPBW and with photometric redshifts where the redshift probability distribution functions, $p(z)$, have $>68\%$ confidence to lie within the ASPECS [C II] frequency coverage are included in our sample. Regarding the latter criterion, we require the 1σ lower and upper limits on the peak redshift, z_{peak} , determined from $p(z)$, to be >6 or <8 , respectively. In total, there are 45 LBGs that satisfy these criteria at $6.1 \leq z_{\text{peak}} \leq 7.6$ with HST F160W band, or H band, magnitudes ranging from the six brightest LBGs in ASPECS with $H_{160} < 27.5 \text{ mag}$ to the faintest at $H_{160} = 30.9 \text{ mag}$, which corresponds roughly to the 5σ depth in XDF. The uncertainty on z_{peak} ranges from $\Delta z_{\text{peak}} = 0.05$ to 0.52 (1σ), with a median value ~ 0.25 across the sample.²³

2.2.1. Properties Derived from SED Fitting

For all LAEs in the sample, we measured the HST photometry in the four WFC3/IR filters (F105W, F125W, F140W, and F160W) from the XDF postage stamps (Illingworth et al. 2013) in $0''.4$ radius apertures. For all LBGs, HST photometry is available from the original selection paper. Additionally, we measured IRAC photometry based on the latest reductions of all the Spitzer/IRAC imaging available in the GOODS field as part of the GREATS survey (M. S. Stefanon et al. 2020, in preparation).

These measurements were used to derive star formation rates as well as photometric redshifts (for the LBGs only) based on spectral energy distribution (SED) fits using the codes EAzy (Brammer et al. 2008) and FAST++ (C. S. Schreiber et al. 2021, in preparation²⁴), respectively. (For the LAEs, the redshift was kept fixed at the $\text{Ly}\alpha$ redshift.) We adopt models from Bruzual & Charlot (2003) with metallicities of $0.2 Z_{\odot}$, constant star formation histories, and a dust law according to Calzetti (1997) to derive SED-based star formation rates for all sources. This approach is very similar to what has been used in Bouwens et al. (2020).

3. Results

3.1. [C II] Search in Optically/Near-IR Selected Galaxies

3.1.1. Ly α Emitters

We obtain Band 6 spectra for the LAEs using a single-pixel extraction (equivalent to an extraction over the area of the

²³ For reference, the minimum and maximum Δz_{peak} correspond to uncertainties of ± 3.1 and $\pm 8.5 \text{ GHz}$, respectively, in the observed frame, centered at the expected frequency for [C II] at z_{peak} .

²⁴ A rewrite of the original FAST IDL code (Kriek et al. 2009) in C++ is available at <https://github.com/cschreib/fastpp>.

²² $\sqrt{\nu_{\text{FWHM}}/\nu_{\text{chn}}} = 1.6$ at band center (242 GHz).

synthesized beam) at the source position determined from HST photometry (Inami et al. 2017); at $6 \lesssim z \lesssim 8$, sources are generally expected to be unresolved by our synthesized beam size of $1''.6 \times 1''.1$ ($= 8.4 \text{ kpc} \times 5.7 \text{ kpc}$ at $z = 7.0$). Due to known astrometric offsets between ALMA and HST data, we measure source coordinates using the Hubble Legacy Field (HLF) reduction of the GOODS-S field that has been shifted to match Gaia data (Whitaker et al. 2019). Comparing positions measured using the original HST coordinates and the Gaia-matched coordinates for our sources, we find median offsets $\Delta(\text{R.A.})_{\text{HST}} = 0''.14$ and $\Delta(\text{decl.})_{\text{HST}} = -0''.24$, consistent with findings from previous ALMA data over this field (Dunlop et al. 2017; Franco et al. 2018). These shifts are smaller than or comparable to the $0''.2$ pixel size in the ASPECS 1 mm image cube.

Resulting spectra are shown in Figure 2 as a function of the offset in velocity units from the $\text{Ly}\alpha$ redshift $z_{\text{Ly}\alpha}$, $\Delta v_{\text{Ly}\alpha} = c(z_{[\text{C II}]} - z_{\text{Ly}\alpha}) / (1 + z_{[\text{C II}]})$, where $z_{[\text{C II}]}$ corresponds to the expected [C II] redshift at the observed frequency. The [C II] line is not detected in any of the six LAEs in our sample. In order to place upper limits on [C II] luminosities for these sources, we first measure the rms in flux density across 8 GHz of bandwidth in the spectrum, centered at the expected frequency for redshifted [C II] emission based on the $\text{Ly}\alpha$ redshift. As in Section 2, we use the fiducial $v_{\text{FWHM}} = 200 \text{ km s}^{-1}$ when converting the rms in flux density to a corresponding limit in line luminosity. Source properties, including our derived limits on [C II] luminosities $L_{[\text{C II}]}$, are summarized in Table 1.

Stacking the six spectra at $\Delta v_{[\text{C II}]} = 0 \text{ km s}^{-1}$, we obtain an average, unweighted MUSE LAE B6 spectrum to search for faint emission. The stack was performed by first blueshifting the B6 spectra to their rest-frame frequencies, adopting either $z_{[\text{C II}]} = z_{\text{Ly}\alpha}$ or $z_{[\text{C II}]} = z_{\text{Ly}\alpha} - \Delta z_{\text{Ly}\alpha}$ for the conversion. Here, $\Delta z_{\text{Ly}\alpha}$ represents an offset between the $\text{Ly}\alpha$ redshift and the systemic redshift of the galaxy, z_{sys} , traced by [C II]. To determine $\Delta z_{\text{Ly}\alpha}$, we follow the approach adopted in ASPECS LP Band 3 CO line stacking (Inami et al. 2020), using the empirical correlation between the FWHM of the $\text{Ly}\alpha$ line profile (measured in Inami et al. 2017) and the redward velocity shift of $\text{Ly}\alpha$ with respect to z_{sys} , presented in Verhamme et al. (2018). For MUSE 852, 6312, 802, 6332, 6524, and 560, the respective $\text{Ly}\alpha$ FWHM = 9.0, 9.4, 4.8, 4.7, 4.0, and 7.0 \AA . The resulting [C II] velocity offsets according to Verhamme et al. (2018) (their Equation (2)) are 230, 250, 120, 110, 89, and 180 km s^{-1} blueward of the $\text{Ly}\alpha$ line peak, or, equivalently, $\Delta z_{\text{Ly}\alpha} = 0.0058, 0.0061, 0.0028, 0.0026, 0.0021$, and 0.0044 . After converting the spectra to the rest frame, each spectrum was linearly resampled onto a reference frequency grid spanning the same velocity range ($\pm 4000 \text{ km s}^{-1}$, or 56.33 GHz on the rest-frame frequency axis) as for the individual spectrum, with velocity resolution chosen to reflect the coarsest resolution of 75.30 km s^{-1} (or 0.4773 GHz in the rest frame) occurring for the source with the highest redshift, MUSE 852. The simple arithmetic average²⁵ of the resampled spectra was used to derive the final stacked spectrum for each choice of $z_{[\text{C II}]}$ (i.e., with and without the velocity shift), presented in Figure 3. At an average redshift $\langle z_{[\text{C II}]} \rangle = 6.29$,

the 5σ rms, $0.61 \text{ mJy beam}^{-1}$, across the full 4000 km s^{-1} bandwidth in the stacked spectrum for $z_{[\text{C II}]} = z_{\text{Ly}\alpha}$ corresponds to an upper limit $L_{[\text{C II}]} < 7.6 \times 10^7 L_{\odot}$.

3.1.2. Lyman-break Galaxies

We have extracted single-pixel spectra in the ASPECS Band 6 data for the 45 Lyman-break selected sources described in Section 2.2. For consistency with the noise estimation on the LAE spectra, we extract spectra in a local bandwidth of 8 GHz, centered at the expected observed frequency for [C II] based on the peak redshift, z_{peak} , from $p(z)$ for a given LBG. In cases where the 1σ uncertainty on z_{peak} is greater than 8 GHz, we use the upper and lower 1σ limits to determine the appropriate frequency range.

No detections are reported. Upper limits on [C II] line luminosity are presented in Table 2 for a subset of the LBG sample containing five of the brightest objects with derived $\text{SFR} \gtrsim 10 M_{\odot} \text{ yr}^{-1}$, roughly corresponding the average 5σ depth in SFR for the ASPECS [C II] survey (see Figure 1).

3.2. Blind [C II] Line Search

A blind search was performed for all spectral lines—including [C II], as well as lower-redshift CO and atomic carbon lines—within the ASPECS LP 1.2 mm survey frequency coverage²⁶ in Decarli et al. (2020). We refer the reader interested in details regarding the blind search algorithm and assessment of reality of blindly detected lines to that work (and references therein), providing here only a brief summary to cover key steps and highlight important changes implemented in the LP analysis since the ASPECS Pilot study (Aravena et al. 2016; Walter et al. 2016).

As described in Decarli et al. (2020), the line search was conducted using the findclumps algorithm (Walter et al. 2016; Decarli et al. 2019; González-López et al. 2019). This algorithm applies a one-dimensional (1D) top-hat convolution in the spectral dimension of the data cube and identifies both positive and negative peaks in the emission, assigning to each peak a signal-to-noise ratio (S/N) calculated by comparing the peak flux density to the rms noise in the map. The width of the top-hat filter is varied iteratively in each convolution to search for spectral features with different line widths. For emission line candidates with $\text{S/N} > 4$, the 1D spectrum is extracted to retrieve a Gaussian-fitted line flux. Line (equivalently, redshift) identification was performed by cross-matching line candidates with ancillary data (e.g., photometric and spectroscopic galaxy catalogs in the HUDF exploited in Sections 3.1.1 and 3.1.2, and/or spectroscopic redshift from the ASPECS 3 mm data set); or, when a line candidate failed to match to a catalog position, the line redshift was assigned on a probabilistic basis, taking into account the cosmic volume sampled by each possible line and various empirical weights reflecting the expected strength of the emission line relative to $\text{CO}(1-0)$.

The fidelity of a line candidate is quantified using a probabilistic approach that compares the number of positive and negative fluctuations, N_{pos} and N_{neg} , in the data for a given

²⁵ An inverse-variance weighted average, where variances were determined channel by channel for each MUSE LAE at their spatial positions in the data cube, was also attempted. The resulting stacked spectrum was similar to the unweighted average, which we have adopted for simplicity.

²⁶ In the on-sky dimension, the search was restricted to the 2.6 arcmin^2 area where the mosaic primary beam response is greater than 50%.

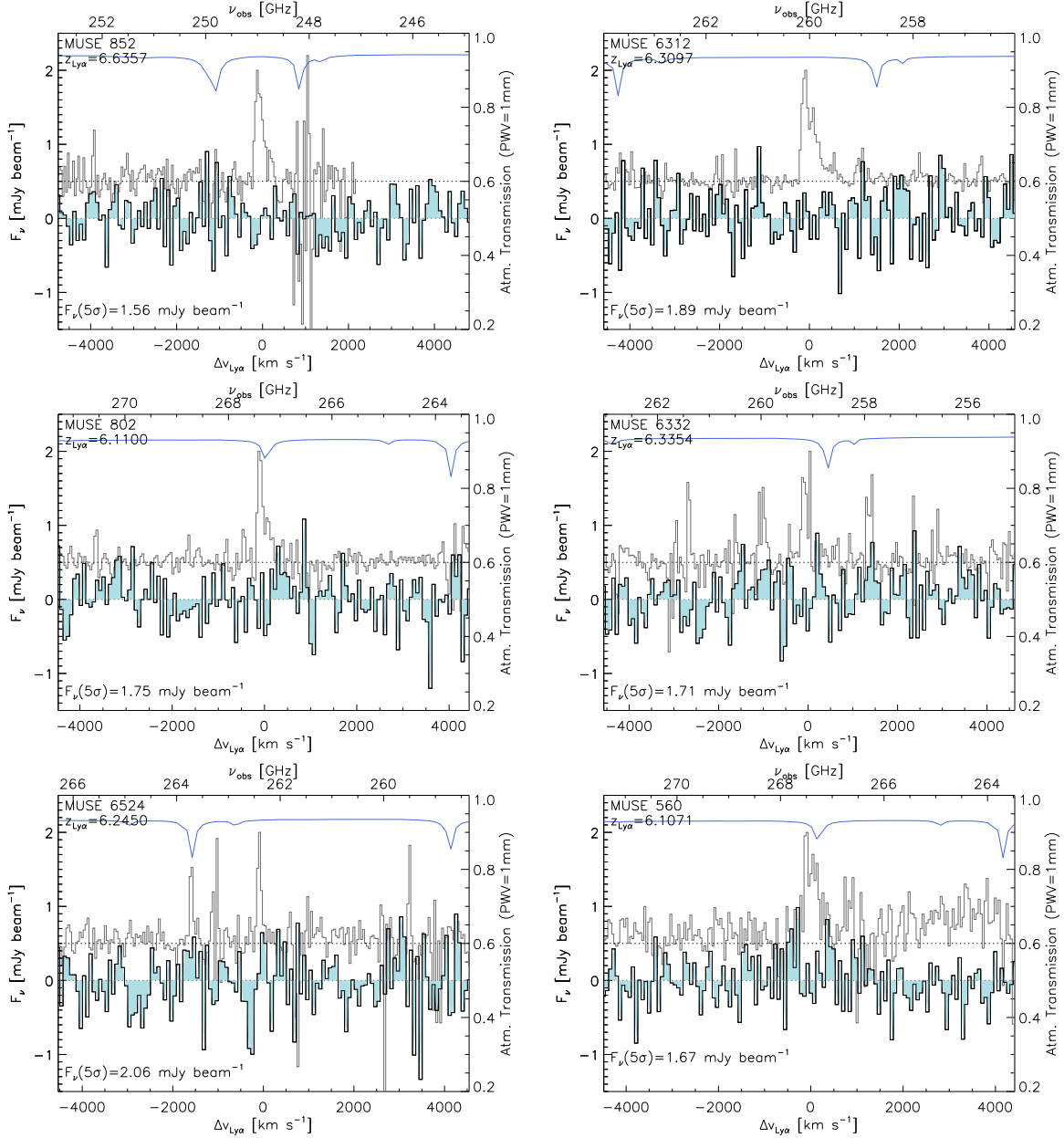


Figure 2. Band 6 spectra ($\Delta\nu_{\text{chn}} = 62.5$ MHz) extracted at positions of known LAEs with secure redshifts ($\text{CONFID} \geq 2$) from Inami et al. (2017) within the ASPECS LP spectral and spatial survey coverage. The Ly α spectrum for each source is overlotted in gray, with arbitrary flux density scaling in each panel. For reference, we also show atmospheric transmission assuming PWV = 1.0 mm (solid blue curve).

S/N and convolution kernel width σ_{kernel} :

$$\text{fidelity} = 1 - \frac{N_{\text{neg}}(\text{S/N}, \sigma_{\text{kernel}})}{N_{\text{pos}}(\text{S/N}, \sigma_{\text{kernel}})}, \quad (1)$$

where the allowable fidelity range from 0 to 1 implies a 100% to 0% chance, respectively, that there are negative line candidates in the data with the same S/N and σ_{kernel} .

This treatment of fidelity improves upon, e.g., the analysis in Aravena et al. (2016), wherein the fidelity of blindly detected [C II] line candidates was expressed as a function of S/N only, given the limited statistical strength, i.e., noise samplings per S/N bin, to test the dependence of fidelity against line width in the Pilot program. As argued in González-López et al. (2019), S/N alone is insufficient to provide an accurate estimate of fidelity in cases where the data potentially contain emission

lines of varying widths, as in ASPECS. Line candidates detected with the same S/N for different spectral convolutions of the data will have different overall significance (not captured by S/N) that depends on the number of independent elements (i.e., frequency channels) in a given convolution. This effect is manifest in the ASPECS 1.2 mm blind line search, and has been presented in Decarli et al. (2020), where the authors found that broader line candidates tend to have higher fidelity than narrower ones at a given S/N (see top panel of their Figure 2).

Only five [C II] line candidates were returned by the blind search performed in Decarli et al. (2020), which yielded a catalog containing a total of 234 line candidates with fidelity > 0.2 . All five of the [C II] candidates have detections with modest S/N ($= 5$ – 6) and low fidelity (< 0.8), with four out of the five candidates characterized by fidelity < 0.5 . We note that the range S/N = 5–6 reflects the threshold where fidelity

Table 1
Source Properties for MUSE LAEs in ASPECS LP

MUSE ID	z	R.A. (deg)	Decl. (deg)	SFR _{SED} ($M_{\odot} \text{ yr}^{-1}$)	$L_{\text{Ly}\alpha}$ ($10^{42} \text{ erg s}^{-1}$)	$L_{[\text{C II}]}$ ($10^8 L_{\odot}$)
(1)	(2)	(3)	(4)	(5)	(6)	(7)
852	6.636	53.169048	−27.778835	$1.20^{+0.09}_{-0.18}$	1.29	<2.24
6312	6.310	53.166118	−27.772048	$4.79^{+3.92}_{-2.16}$	5.03	<2.47
802	6.110	53.168540	−27.775677	$0.18^{+0.04}_{-0.03}$	1.45	<2.15
6332	6.335	53.158161	−27.778554	$0.12^{+0.42}_{-0.05}$	1.28	<2.25
6524	6.245	53.158247	−27.767763	$0.16^{+0.51}_{-0.10}$	0.66	<2.64
560	6.107	53.159523	−27.771524	$13.49^{+10.50}_{-5.90}$	1.48	<2.05

Note. (1) MUSE ID from Inami et al. (2017). (2) Ly α redshift, determined for the peak flux of the Ly α profile (3), (4) R.A. and decl. determined from the Hubble XDF Y-band (F105W) image, including spatial offsets from Gaia-matched reduction of the HLF GOODS-S images. (5) SED-based SFR estimate. (6) Ly α luminosity in units of $10^{42} \text{ erg s}^{-1}$ (Inami et al. 2017). (7) Upper limit (5σ) on [C II] luminosity, in units of $10^8 L_{\odot}$, assuming FWHM = 200 km s $^{-1}$.

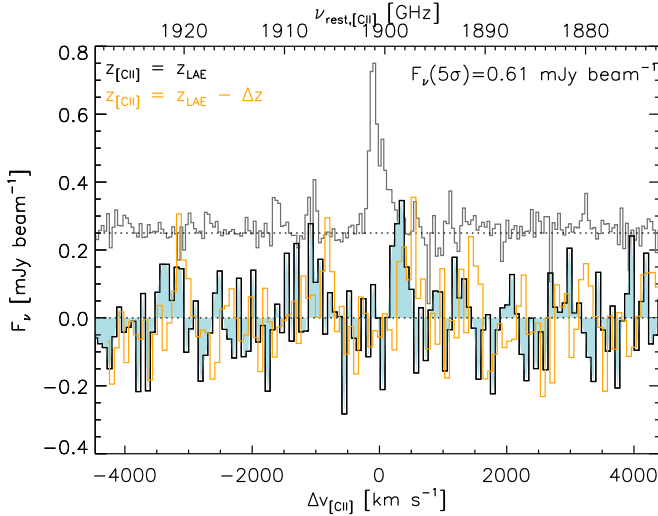


Figure 3. Stacked B6 spectra for the six MUSE LAEs in ASPECS, assuming that the [C II] redshift matches exactly the Ly α redshift (blue filled curve) or an empirically derived systemic redshift according to Verhamme et al. (2018) (orange curve). The stacked Ly α spectrum is also shown for comparison (gray curve), with arbitrary flux density normalization. The 5σ rms $F_v(5\sigma) = 0.61 \text{ mJy beam}^{-1}$ reported here refers to the B6 stacked spectrum computed without a velocity offset for the [C II] line.

rapidly decreases to zero (Figure 2, Decarli et al. 2020). Only one [C II] line candidate is considered a good match²⁷ to a known optical/near-IR counterpart with a photometric redshift, but, based on the analysis above, the probability that the line is spurious is >70% (i.e., fidelity = 0.28). We therefore discount it, along with the remaining [C II] line candidates, upon inspecting their Band 6 spectra and continuum postage stamps.

3.3. Continuum Emission: Individual Sources and Stack

In addition to extracting spectra for the MUSE LAEs described in Section 3.1.1, we have also searched for the presence of continuum emission at the corresponding locations in the line-free 1.2 mm map obtained in González-López et al. (2020). Continuum image cutouts ($5'' \times 5''$; no primary beam correction) centered at individual LAE positions are shown in Figure 4(a), with S/N contours overlaid after adopting an rms value of $9.3 \mu\text{Jy beam}^{-1}$ (González-López et al. 2020).

²⁷ Here, we require that the [C II] line candidate at $z_{[\text{C II}]}$ and the known source at z have (1) a spatial offset within $0''.1$ and (2) a redshift separation $(z - z_{[\text{C II}]})/(1 + z) < 0.1$.

MUSE 6312 is the only source with plausible continuum emission, observed at the 2σ – 2.5σ level, but improved sensitivity is needed to assert the reality of this emission. We can improve our sensitivity to the average 1.2 mm continuum emission for all the LAEs in our sample by stacking. In Figure 4(b), we show the results of a continuum stack on the central location of the six MUSE LAEs, generated by averaging the emission in continuum images and weighting each pixel by the mosaic sensitivity pattern. The stacked continuum image has an rms noise equal to $2.98 \mu\text{Jy beam}^{-1}$. Nondetections of 1.2 mm continuum flux in individual LAEs with comparable $L_{\text{Ly}\alpha}$ ($\lesssim 5 \times 10^{42} \text{ erg s}^{-1}$) at similar redshift have been previously reported down to ~ 10 – $15 \mu\text{Jy}$ (1σ) (e.g., Knudsen et al. 2016; Bradač et al. 2017).

We can use the nondetection of continuum in the stack to place an upper limit on the dust-obscured SFR in the LAEs. Adopting a dust temperature of 30 K (50 K) and emissivity index $\beta = 1.6$, we integrate a modified blackbody spectrum across the far-infrared (FIR) wavelengths 42.5 – $122.5 \mu\text{m}$ (Helou et al. 1988) to place an upper limit (3σ) on the FIR luminosity $L_{\text{FIR}} < 2.7 \times 10^9 L_{\odot}$ ($1.2 \times 10^{10} L_{\odot}$) for these sources.²⁸ (We have adopted an emissivity index and dust temperatures consistent with findings for $z \sim 5.5$ galaxies in Faisst et al. 2020.) Using the conversion $\text{SFR}/L_{\text{FIR}} = 1.5 \times 10^{-10} M_{\odot} \text{ yr}^{-1} L_{\odot}^{-1}$ (for Chabrier IMF, as in Carilli & Walter 2013), we find IR-based $\text{SFR} < 0.4 M_{\odot} \text{ yr}^{-1}$ ($1.8 M_{\odot} \text{ yr}^{-1}$).

Low to negligible levels of obscured star formation in the MUSE LAEs are consistent with results from a related independent study of 1.2 mm continuum emission from ~ 1400 galaxies with either Lyman-break or photometric redshift selection at $z = 1.5$ – 10 in the ASPECS LP 4.2 arcmin^2 footprint (Bouwens et al. 2020). The authors there—and in the ASPECS 1.2 mm blind search for a continuum source (González-López et al. 2020)—do not report any continuum detections beyond $z = 4$ for their sample of UV-selected galaxies, which includes the LBGs of Bouwens et al. (2015) used in this work; we can confirm nondetections for these overlapping sources after examining the corresponding 1.2 mm continuum postage stamps. Bouwens et al. (2020) also

²⁸ While the higher temperatures of the cosmic microwave background (CMB) at the redshifts relevant to this analysis can reduce detectability of the intrinsic continuum flux density or provide additional dust heating (da Cunha et al. 2013), we follow the reasoning in, e.g., Willott et al. (2015), and argue that—with a single flux density measurement—these competing effects of the CMB background are poorly constrained.

Table 2
Source Properties for LBGs in ASPECS LP with $\text{SFR}_{\text{SED}} > 10 M_{\odot} \text{ yr}^{-1}$

ID	z	R.A.	Decl.	SFR_{SED}	$L_{[\text{C II}]}$
(1)	(2)	(deg)	(deg)	($M_{\odot} \text{ yr}^{-1}$)	($10^8 L_{\odot}$)
XDFI-2374646327	6.48 ± 0.07	53.156096	-27.775775	48^{+8}_{-9}	<2.0
XDFZ-2425646566	6.83 ± 0.06	53.177333	-27.782389	26^{+6}_{-4}	<2.6
XDFY-2395371744	7.58 ± 0.10	53.164733	-27.788178	20^{+7}_{-3}	<2.4
XDFY-2388047071	7.54 ± 0.10	53.161683	-27.785322	19^{+3}_{-7}	<2.1
GSDI-2382846172	6.08 ± 0.08	53.159504	-27.771450	12^{+5}_{-4}	<2.2

Note. (1), (2) ID and photometric redshift from Bouwens et al. (2015). (3) R.A. (4) Decl. (5) SED-based SFR estimate from FAST++. (6) Upper limit (5σ) on [C II] luminosity, in units of $10^8 L_{\odot}$, assuming $\text{FWHM} = 200 \text{ km s}^{-1}$.

searched for 1.2 mm continuum flux in a stack of low-mass ($<10^{9.25} M_{\odot}$) galaxies across the full redshift range probed by their sample, finding an average 1.2 mm continuum flux density of $-0.1 \pm 0.4 \mu\text{Jy}$ for the 1253 galaxies in the stack, implying that the obscured SFR in these galaxies is approximately zero (assuming $z = 4$ for the entire stack).

4. Discussion

In this section, we compare our findings in Sections 3.1–3.2 to the results of the [C II] line search in the ASPECS Pilot study (Aravena et al. 2016), and place the findings of the targeted [C II] searches on LAEs and LBGs in ASPECS (Sections 3.1.1 and 3.1.2) in the context of empirical and predicted $L_{[\text{C II}]}$ –SFR relations at $z \sim 0$ and $6 \leq z \leq 8$. Finally, we use the absence of reliable detections in the blind search to place upper limits on the cumulative [C II] source densities.

4.1. Comparison to ASPECS Pilot

Aravena et al. (2016) presented the results of a [C II] line search in the ASPECS Pilot survey (Walter et al. 2016). As the precursor to the Large Program, ASPECS Pilot shared the same survey strategy (e.g., array configuration, frequency setups, comparable survey depth) as ASPECS LP, but targeted a smaller, 1 arcmin² patch of sky within the HUDF. The final mean rms noise achieved was $0.42 \text{ mJy beam}^{-1}$ per 62.5 MHz channel, roughly constant across the survey bandwidth, which is a factor 1.4 higher than the mean rms of $0.30 \text{ mJy beam}^{-1}$ per 62.5 MHz channel for ASPECS LP due to more favorable weather conditions in the latter campaign.

The blind line search in the lower-sensitivity ASPECS Pilot data cube returned 14 [C II] line candidates down to a lower S/N threshold (~ 4.5) than considered in the LP blind search. Fidelities were obtained in a similar probabilistic fashion as expressed in Equation (1), but lacking the dependence on line width: $\text{fidelity} = 1 - N_{\text{neg}}(\text{S/N})/N_{\text{pos}}(\text{S/N})$. Two of these candidates were not associated with known nearby optical dropout galaxies (at any redshift), and were presented based on an assessment of their fidelities ($>70\%$), with the caveat that one line candidate overlapped with an atmospheric absorption feature, and that further ALMA spectroscopy would be needed to confirm the candidates’ reality. The remaining 12 candidates were found after applying positional priors—set by their proximity ($<1''$) to optical dropout galaxies at $5.5 < z < 8.5$ —to the blindly detected line candidates, and setting a lower threshold to the fidelity ($>40\%$), given the associations with optical counterparts.

Because 13 of the 14 line candidates lie within the ASPECS LP HPBW, we extract their spectra from the peak pixel position reported in Aravena et al. (2016) (see their Table 2) in the LP data cube to independently confirm or reject the presence of line emission.²⁹ The new observations disprove the reality of all 13 candidates. These nondetections reinforce the fact that even line candidates with optical associations at the $4.5 < \text{S/N} < 5.5$ level can be mistaken for real sources, and motivate (1) the development of improved techniques for assessing the line fidelity, and (2) the adoption of a more conservative approach (i.e., setting higher flux thresholds) when presenting line candidates, as described, e.g., in Section 3.2 and references therein.

4.2. $L_{[\text{C II}]}$ –SFR Relation at $6 \leq z \leq 8$

Figure 5 shows the upper limits (5σ) on $L_{[\text{C II}]}$ measured for MUSE LAEs and LBGs in ASPECS as a function of their inferred total SFRs, including unobscured and, where available, obscured SFR contributions. For comparison, we include literature data for [C II] observations in the redshift range $z = 6$ – 7 compiled by Matthee et al. (2019), wherein the authors recalculated SFRs for the entire sample in a consistent manner, setting a standard IMF (Salpeter) and dust temperature (45 K) for all galaxies. For consistency with our derived SFRs, which assumed a Chabrier IMF, we multiply their UV- and IR-based SFR values by IMF conversion factors equal to 0.63 and 0.87, respectively (Madau & Dickinson 2014).

Here, the depicted error on SFR for the LAE sample includes the uncertainty associated with the SED fitting, as well as a 5σ upper limit on dust-obscured SFR ($= 7.6$ – $10.2 M_{\odot} \text{ yr}^{-1}$) derived from the extrapolation of total IR luminosity ($L_{\text{IR}}[8$ – $1000 \mu\text{m}]$) from the 1.2 mm continuum data. To be consistent with the plotted literature data points, we adopt the same modified blackbody (MBB) parameters and L_{IR} –SFR conversion factor as in Matthee et al. (2019) when estimating L_{IR} and the SFR. (Note that the MBB parameters used in Matthee et al. (2019) differ slightly from the chosen parameters in Section 3.3.³⁰) We do not show individual uncertainties on

²⁹ One source in Aravena et al. (2016), ID30, lies in a region where the LP mosaic sensitivity is $\sim 30\%$, so we do not formally include it in the results of this study, after visually inspecting the data.

³⁰ Specifically, instead of our adopted dust temperatures at 30 and 50 K and $\beta = 1.6$, Matthee et al. (2019) adopt a single 45 K dust temperature and $\beta = 1.5$. As an example comparison, the latter parameterization results in roughly 0.65 times lower IR luminosity than the MBB with 50 K dust temperature and $\beta = 1.6$, when integrating over the same wavelength range from 8 to 1000 μm .

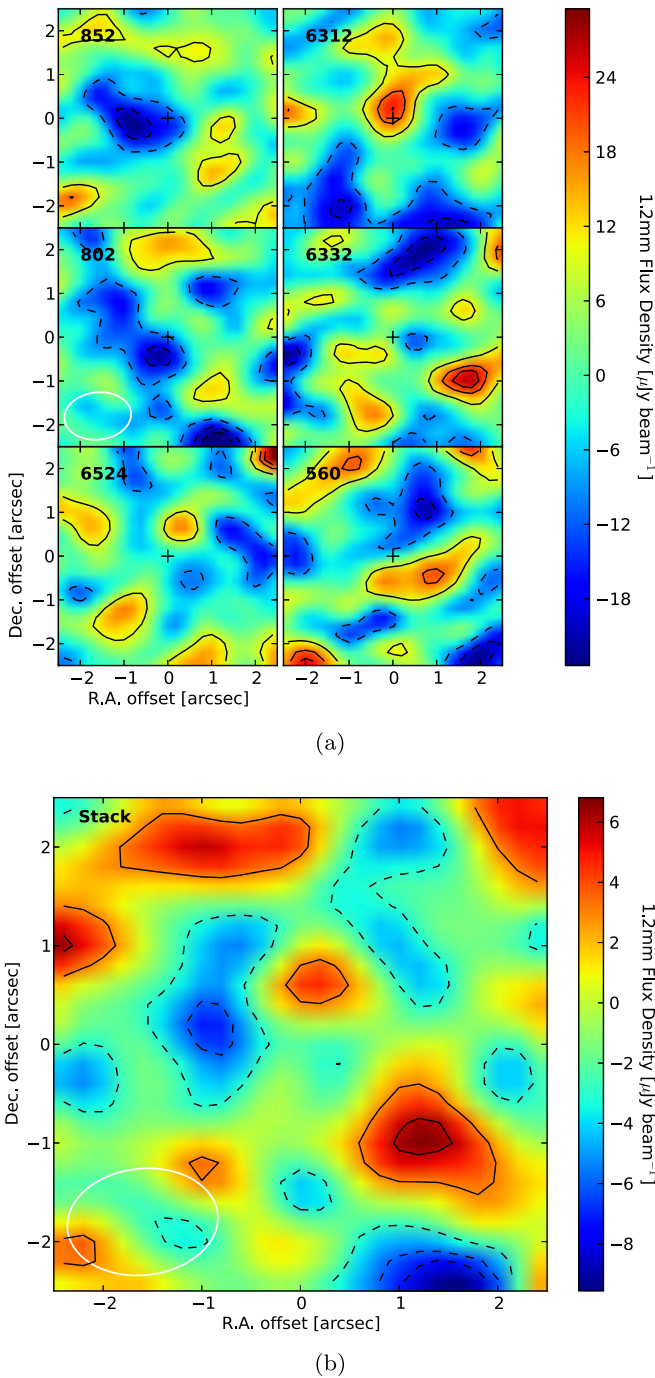


Figure 4. (a) $5'' \times 5''$ postage stamps of 1.2 mm continuum images (without PB correction) centered at locations of MUSE LAEs in ASPECS. The LAE position in each cutout is indicated with a “+” symbol; refer to Table 1 for sky coordinates. (b) Mean 1.2 mm continuum emission obtained by stacking on the locations of the six MUSE LAEs shown in panel (a). Contours in both panels represent the emission at 1.0σ ($= 9.3 \mu\text{Jy beam}^{-1}$), 2.0σ , and 2.5σ levels, with dashed and solid contours corresponding to negative and positive flux densities, respectively. For reference, the synthesized beam is shown as an ellipse in the bottom left corners of the postage stamp for MUSE 802 and the stack.

SFR for the LBG sample; the uncertainties are comparable to what was found for the MUSE LAEs.

For sources with SFRs less than a few $M_{\odot} \text{ yr}^{-1}$, the ASPECS LP nondetections are unsurprising based on the $L_{[\text{C II}]}$ –SFR relation calibrated for local galaxies (De Looze et al. 2014). In the literature, the only [C II] detections reported in this SFR

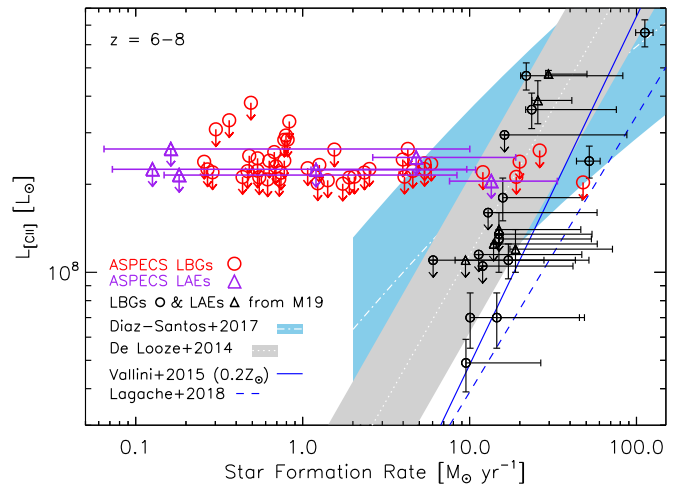


Figure 5. $L_{[\text{C II}]}$ –SFR relation at $z > 6$, with data points distinguished by target selection: circle and triangle symbols reflect galaxies initially discovered as LBGs and LAEs, respectively. 5σ upper limits on $L_{[\text{C II}]}$ are presented for LBGs (red circles) and MUSE LAEs (purple triangles) within the ASPECS HPBW and redshift coverage. Detections and 5σ upper limits from the literature, as compiled by Matthee et al. (2019), are shown for comparison as black symbols. Also shown are the local $L_{[\text{C II}]}$ –SFR relations calibrated by De Looze et al. (2014) for H II regions/star-forming systems, including starbursts (dark gray band; 1σ dispersion = 0.27 dex), and by Díaz-Santos et al. (2017) for (ultra) luminous IR galaxies (light blue band; 1σ); white dotted lines within each band indicate the best-fit relations for each sample. Theoretical predictions for the $L_{[\text{C II}]}$ –SFR relation at $z = 6$ –7 are plotted from Vallini et al. (2015) and Lagache et al. (2018) (solid and dashed blue linestyles, respectively).

regime are targeted ALMA observations of an LBG (Knudsen et al. 2016) and LAE (Bradač et al. 2017) where emission has been magnified by strong gravitational lensing.³¹

There are, however, a few LBGs within the survey HPBW where the ASPECS [C II] detection threshold is more constraining. Explicitly, if we set for ASPECS the mean 5σ survey depth on SFR based on the locally calibrated $L_{[\text{C II}]}$ –SFR relation of De Looze et al. (2014) (using their “star-forming H II region/starburst” sample), then detections might have been expected for galaxies with $\text{SFR} \geq 16 \pm 8 M_{\odot} \text{ yr}^{-1}$ ($\text{SFR} \geq 32 \pm 18 M_{\odot} \text{ yr}^{-1}$) at $z = 6$ ($z = 8$), where the error bars reflect the uncertainty in the $L_{[\text{C II}]}$ –SFR relation. We motivate the choice of the local $L_{[\text{C II}]}$ –SFR relation to set a fiducial survey depth in SFR in the light of results of Schaerer et al. (2020), who find little to no evolution in the local $L_{[\text{C II}]}$ –SFR relation since $z \leq 6$, because the consensus at $z > 6$ on the nature (e.g., its slope, scatter, and linearity) of this relation has not converged.

For instance, the 5σ upper limit on [C II] luminosity in XDFI-2374646327—the LBG in ASPECS with the highest observed SFR ($\sim 50 M_{\odot} \text{ yr}^{-1}$)—is $L_{[\text{C II}]} < 2.0 \times 10^8 L_{\odot}$, which is more than three times lower than expected from the best-fit relation for local star-forming galaxies according to De Looze et al. (2014), and is also below the observed 0.27 dex scatter in the relation of De Looze et al. (2014) (gray-shaded band in Figure 5). The limit is consistent, however, with the locally calibrated $L_{[\text{C II}]}$ –SFR relation in Díaz-Santos et al. (2013, 2017), where a turnover in $L_{[\text{C II}]}$ is observed for galaxies with $\text{SFR} \gtrsim 30 M_{\odot} \text{ yr}^{-1}$. The discrepancy between the two locally calibrated relations is partly explained by the fact

³¹ After correcting for a lensing magnification factor of 5, the LAE in Bradač et al. (2017) has $L_{\text{Ly}\alpha} = 1.3 \times 10^{42} \text{ erg s}^{-1}$, which is comparable to the range of Ly α luminosities probed by the MUSE LAEs in ASPECS.

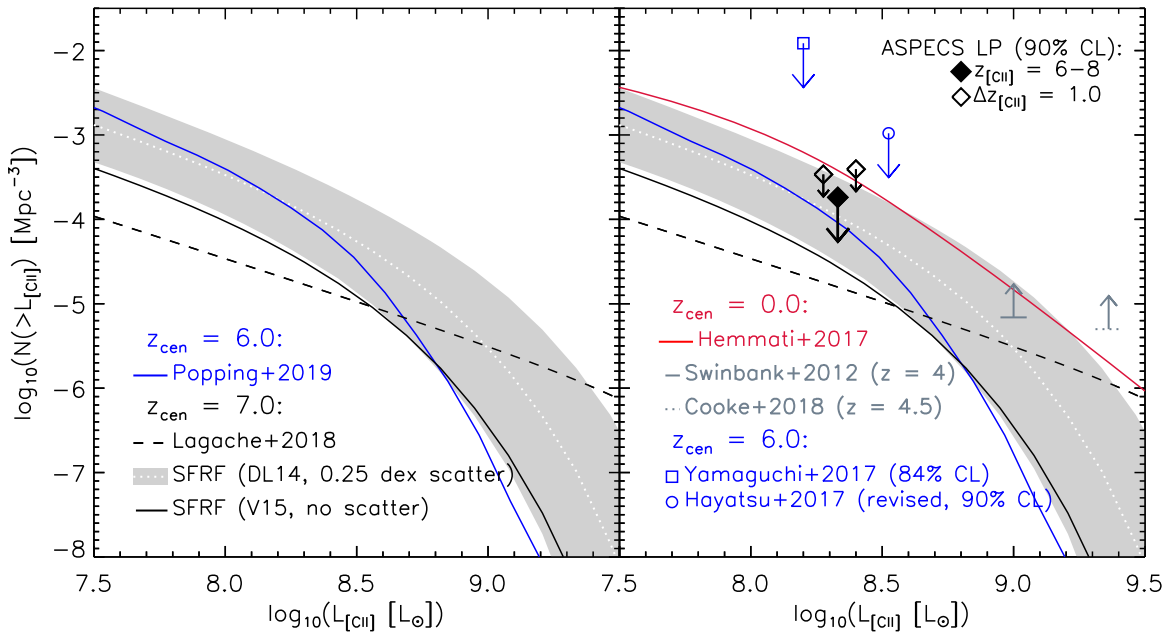


Figure 6. Left: theoretical predictions for $N(>L_{\text{CII}})$ vs. L_{CII} at $z = 6$ (blue curve: Popping et al. 2019) and $z = 7$ (white dotted curve: best fit for simulated number densities based on the SFRF of Smit et al. (2016) convolved with the L_{CII} –SFR relation from the H II region/starburst calibration of De Looze et al. (2014), including a 0.25 dex scatter on L_{CII} –SFR shown as the gray band; black solid curve: same as white dotted curve, except using the L_{CII} –SFR relation from Vallini et al. (2015) ($0.2 Z_{\odot}$); black dashed curve: Lagache et al. (2018)). Right: observational constraints on $N(>L_{\text{CII}})$ vs. L_{CII} , with upper limits (90% confidence level) derived from the full ASPECS survey volume covering $z = 6-8$ (filled black diamond) and the literature at $z \sim 6$ (Hayatsu et al. 2017; Yamaguchi et al. 2017). The [C II] cumulative number densities measured at $z \sim 0$ (Hemmati et al. 2017) and lower limits at $z \sim 4-5$ (Swinbank et al. 2012; Cooke et al. 2018) are plotted as the gray arrows. Theoretical predictions from the left panel are underlaid to facilitate comparison.

that the SFR surface densities ($\sim 85 M_{\odot} \text{ yr}^{-1} \text{ kpc}^{-2}$) probed in the GOALS sample of Díaz-Santos et al. (2013, 2017) are nearly 2–3 times higher than in the objects compiled by De Looze et al. (2014) and other local galaxy samples (e.g., Herrera-Camus et al. 2015). Thus, one possible explanation for the [C II] deficiency in this source could be the presence of a high surface density of star formation, which is supported, e.g., by findings in Ferrara et al. (2019), who predict a deficiency in [C II] luminosity surface density with respect to the relation of De Looze et al. (2014) for galaxies at $z > 5$ with SFR surface densities above $\sim 85 M_{\odot} \text{ yr}^{-1} \text{ kpc}^{-2}$. Other factors, such as metallicity, as proposed, e.g., in Vallini et al. (2015), might also play a role, though we note that a saturation of [C II] emission in systems with high SFR surface density is predicted to be dominant over the effects of metallicity (Ferrara et al. 2019).

Excluding XDFI-2374646327, the derived upper limits for the remaining sources with $\text{SFR} \gtrsim 10 M_{\odot} \text{ yr}^{-1}$ in ASPECS are consistent with the observed scatter in previous targeted ALMA observations, as well as with the local L_{CII} –SFR relations calibrated by Díaz-Santos et al. (2013) and De Looze et al. (2014).

4.3. Cumulative [C II] Source Densities at $6 \leq z \leq 8$

Figure 6 shows the upper limits (downward-pointing arrows) on the cumulative [C II] source densities (i.e., number density of [C II] emitters with luminosity greater than L_{CII}) derived from the ASPECS LP blind search. The choice of presenting cumulative [C II] source densities is for consistency with Aravena et al. (2016); Figure 6, and also Figure 5 from Section 4.2, replace the results of that work. We present limits at 90% confidence level assuming Poisson statistics for zero detections (Gehrels 1986) for the full survey volume spanning $z = 6-8$, as well as for smaller volumes corresponding to

redshift ranges $z = 6-7$ and $z = 7-8$.³² The ASPECS [C II] luminosity depths (rightward-pointing arrows) are the 5σ upper limits derived from the average rms per channel in the data cube across the relevant frequency ranges for each bin³³ (Figure 1). Table 3 summarizes the measured limits for the different redshift ranges. We note that Decarli et al. (2020) present upper limits on the [C II] luminosity function (in units of $\text{Mpc}^{-3} \text{ dex}^{-1}$) in ASPECS 1.2 mm data, derived using the blind search algorithm developed there (and in references therein) for CO and other lines within the ASPECS survey bandwidth. To facilitate comparison, we convert the 3σ limits on the luminosity function presented in their Table 4 to the appropriate number of Gaussian σ equivalent to the 90% confidence level ($\approx 1.3\sigma$), and integrate the resulting limits to arrive at a cumulative number density of $< 1.94 \times 10^{-4} \text{ Mpc}^{-3}$ for [C II] emitters with luminosities greater than their lowest luminosity bin centered at $L'_{\text{CII}} = 1.26 \times 10^9 \text{ K km s}^{-1} \text{ pc}^2$, or $L_{\text{CII}} = 2.77 \times 10^8 L_{\odot}$.

We show for comparison the previous observational constraints at $z \sim 6$ in the literature from Hayatsu et al. (2017)³⁴ and Yamaguchi et al. (2017). The [C II] number counts observed for local galaxies (Hemmati et al. 2017) are also shown (solid red curve). The ASPECS limits on the cumulative source densities imply that the [C II] number

³² As in Gehrels (1986), the 1.0σ , 1.3σ , 2.0σ , and 3.0σ limits in Gaussian statistics correspond to single-sided Poissonian upper limits at confidence levels of 84.1%, 90.0%, 97.5%, and 99.9%, respectively. The Gaussian 3σ upper limit, for example, can be derived for ASPECS by multiplying the upper limit for zero detections quoted at 90% confidence level by a factor 2.869.

³³ After adopting the central redshift corresponding to each redshift bin.

³⁴ The authors in Hayatsu et al. (2019) show the detections in Hayatsu et al. (2017) to be spurious, so we have remeasured upper limits (90% confidence level) for Hayatsu et al. (2017), adopting a mean rms noise of $0.8 \text{ mJy beam}^{-1}$ per 36 km s^{-1} channel and survey volume $2.2 \times 10^3 \text{ Mpc}^{-3}$.

Table 3
Limits on Cumulative [C II] Source Densities

z Range	$n(>L_{[\text{C II}]})$ (Mpc^{-3})	$L_{[\text{C II}]}$ (L_{\odot})	References
(1)	(2)	(3)	(4)
6–8	$<1.82 (5.22) \times 10^{-4}$	$>2.14 \times 10^8$	U21
6–8	$<1.94 (4.47) \times 10^{-4}$	$>2.77 \times 10^8$	D20
6–7	$<3.40 (9.75) \times 10^{-4}$	$>1.89 \times 10^8$	U21
7–8	$<3.93 (11.3) \times 10^{-4}$	$>2.51 \times 10^8$	U21

Note. (1) Redshift range. (2) Upper limit at 90% (99.9%) confidence level on cumulative number densities. For D20, tabulated 3σ upper limits on the [C II] luminosity function (in units of $\text{Mpc}^{-3} \text{dex}^{-1}$) have been converted to 1.3σ upper limits in each luminosity bin to derive an equivalent one-sided Poissonian limit on the integrated, cumulative [C II] source densities at 90% confidence level. No conversions on the upper limits in D20 were performed in the case of the Poissonian upper limit quoted at 99.9% confidence level, which corresponds to the 3σ limit in Gaussian statistics. (3) [C II] luminosity depth (5σ). (4) Reference (U21: this work; D20: Decarli et al. 2020).

density is at least a factor of 2 lower than measured at $z \sim 0$ at the ASPECS 5σ $L_{[\text{C II}]}$ depth of $2.14 \times 10^8 L_{\odot}$. At intermediate redshifts $z \sim 4$ –6, the ALPINE survey also provides constraints on [C II] number counts (Yan et al. 2020; Loiacono et al. 2021), though a direct comparison with ASPECS results, or any [C II] number counts that originate from flux-limited surveys (like the GOALS+RBGS sample in Hemmati et al. 2017), is complicated by the nature of the target selection (Le Fèvre et al. 2020) in that survey sample.

The cumulative [C II] source densities can indicate whether the current understanding of the $L_{[\text{C II}]}$ –SFR relation at high redshift established by previous targeted ALMA studies of individual optically selected sources is consistent with the results of the ASPECS [C II] blind search. The white dotted curve in Figure 6 represents the best fit to simulated [C II] number counts at $z=7$, generated using a Monte Carlo simulation that predicts the number density of [C II] emitters at a given $L_{[\text{C II}]}$ and SFR by sampling the star formation rate function (SFRF, in units of $M_{\odot} \text{yr}^{-1} \text{Mpc}^{-3}$) measured in GOODS-N and -S from Smit et al. (2016) and applying the $L_{[\text{C II}]}$ –SFR relation for galaxies from De Looze et al. (2014). The simulations account for uncorrelated errors in the SFRF Schechter parameters and include a 0.25 dex scatter in $L_{[\text{C II}]}$ –SFR (gray band in Figure 5); the inclusion of correlated errors in the SFRF Schechter parameters would decrease the overall dispersion in the simulations (gray swath in Figure 6; 1σ). Note that the UV-based SFRFs have been corrected for dust extinction using an SMC-like attenuation law; the actual attenuation law is more likely to lie between the SMC curve and a Calzetti law (Bouwens et al. 2020). Our deepest upper limit (90% confidence level) on the cumulative number density (centered at $z=7$) does not rule out the best fit to this simulated model, but begins to place useful constraints on the predicted scatter, driven largely by the dispersion in $L_{[\text{C II}]}$ –SFR; it is important to note, however, that the reported upper limit in this work neglects the effect of cosmic variance. If we replace the $L_{[\text{C II}]}$ –SFR relation of De Looze et al. (2014) in our simulation with the prescription found in Vallini et al. (2015), then the resulting average fit is the solid black curve in the same figure, which is roughly 1 dex below our upper limit. Thus, while the blind search is unbiased and could potentially reveal a population of [C II] emitters that are not identified via optical selections, our results in Figure 6 indicate that the [C II] number

density at $6 \leq z \leq 8$ in the HUDF is broadly consistent with expectations based on the current understanding obtained by targeted observations of LAEs and LBGs (Figure 5).

Additional theoretical models at $z=6$ (Popping et al. 2019) and $z=7$ (Lagache et al. 2018) are also plotted, for comparison (Figure 6, left panel).

4.4. Cosmic Molecular Gas Mass Density

Using [C II] as a molecular gas tracer (Zanella et al. 2018), we complement the recent measurements of cosmic molecular gas density, ρ_{H_2} , presented in the ASPECS study by Decarli et al. (2020) (their Figure 9), extending these constraints to $z > 6$. At this redshift, the COLDz survey, which targeted CO emission from 30 to 39 GHz with the Very Large Array, places the only existing constraints on ρ_{H_2} (Riechers et al. 2019).

We here use, for the purpose of a rough estimate, the $L_{[\text{C II}]}$ – H_2 conversion factor, $\alpha_{[\text{C II}]} = 31 M_{\odot} L_{\odot}^{-1}$, empirically calibrated in Zanella et al. (2018), to guide our estimate of ρ_{H_2} . We refer the interested reader to that work (and references therein) for thorough discussion of related caveats on the reliability of [C II] as a molecular gas tracer, e.g., its prevalence in different ISM phases. This value for $\alpha_{[\text{C II}]}$ appears to be invariant (within a scatter of 0.3 dex) across the different samples explored in their work, including local main-sequence (MS) and starbursting galaxies, low-metallicity local dwarfs, and high-redshift ($z \sim 2$ –5.5) MS and starburst galaxies.

Per our deepest constraints on the total number density of [C II] emitters for the $z=6$ –8 redshift bin (Table 3), the [C II] luminosity density for all galaxies above our 5σ depth in $L_{[\text{C II}]}$ at this redshift cannot exceed $(2.14 \times 10^8 L_{\odot}) \times (1.82 \times 10^{-4} \text{Mpc}^{-3}) = 3.89 \times 10^4 L_{\odot} \text{Mpc}^{-3}$. This implies that ρ_{H_2} from galaxies with $L_{[\text{C II}]} > 2.14 \times 10^8 L_{\odot}$ cannot exceed $\alpha_{[\text{C II}]} \times (3.89 \times 10^4 L_{\odot} \text{Mpc}^{-3}) = 1.2 \times 10^6 M_{\odot} \text{Mpc}^{-3}$. Comparing with constraints on ρ_{H_2} from the COLDz survey (Riechers et al. 2019), we find that our upper limit sits just below the measured range of their CO-derived estimate of $\rho_{\text{H}_2} = (0.14$ – $1.1) \times 10^7 M_{\odot} \text{Mpc}^{-3}$ in the $z=4.9$ – 6.7 redshift bin. While assumptions regarding, e.g., the CO– H_2 conversion factor outlined in Riechers et al. (2019) and the uncertain nature of the $\alpha_{[\text{C II}]}$ factor applied in the context of this work are likely dominant sources of this discrepancy, we point out that (1) the COLDz measurement reflects contributions from galaxies at lower redshift than in ASPECS, and (2) there might be non-negligible contributions to the [C II] luminosity density, and thus ρ_{H_2} , from lower-luminosity [C II] emitters, depending on the faint-end slope of the [C II] luminosity function at $z \sim 7$.

5. Conclusions

We present a targeted search for [C II] emission from optically selected galaxies within the ASPECS LP 1.2 mm data cube ($\nu_{\text{obs}} = 212$ – 272 GHz), as well as the deepest constraints on the number density of [C II] emitters at the end of reionization, from $z=6$ –8. Key results include the following.

- (i) With a mean rms sensitivity of $0.30 \text{ mJy beam}^{-1}$ per 62.5 MHz channel across the full ASPECS B6 bandwidth—corresponding to average 5σ depths in $L_{[\text{C II}]} = 2.14 \times 10^8 L_{\odot}$ and $\text{SFR} \sim 20 M_{\odot} \text{yr}^{-1}$ (according to De Looze et al. 2014)—we place upper limits on [C II] line luminosity for six LAEs and 45 LBGs within the ASPECS HPBW (2.9 arcmin^2). For these sources, the

derived upper limits are consistent with previous targeted ALMA observations of $z = 6\text{--}7$ LAEs and LBGs, as well as the local $L_{[\text{C II}]}$ -SFR relations from De Looze et al. (2014) or, in the case of a single LBG with estimated SED-based SFR $\sim 50 M_{\odot} \text{ yr}^{-1}$, from Díaz-Santos et al. (2017).

- (ii) Upon stacking the 1.2 mm continuum data for the six LAEs in our survey field, we can probe emission down to an rms noise level equal to $2.98 \mu\text{Jy beam}^{-1}$. Adopting a template modified blackbody spectrum with a dust temperature of 50 K, $\beta = 1.6$, and integrating from FIR wavelengths $42.5\text{--}122.5 \mu\text{m}$, we place a 3σ upper limit on $L_{\text{FIR}} < 1.2 \times 10^{10}$ and $\text{SFR} < 1.8 M_{\odot} \text{ yr}^{-1}$ (or $L_{\text{FIR}} < 2.7 \times 10^9$ and $\text{SFR} < 0.4 M_{\odot} \text{ yr}^{-1}$ for a dust temperature of 30 K).
- (iii) In a volume of $\sim 12,500$ comoving Mpc^3 , we find that the number density of [C II] emitters with line luminosity greater than $2.14 \times 10^8 L_{\odot}$ in the redshift range $z = 6\text{--}8$ is less than $1.82 \times 10^{-3} \text{ Mpc}^{-3}$ (90% confidence level), consistent with results in Decarli et al. (2020), who performed a blind line search for all spectral lines within ASPECS spectral coverage. Our upper limits indicate evolution of the [C II] LF from $z = 6\text{--}8$ to $z = 0$ at the quoted [C II] depth for ASPECS.








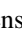

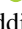




Looking forward, there are different avenues to make further progress in this field. One promising avenue would be to obtain significantly deeper [C II] and dust continuum observations of individual reionization sources that are selected using various techniques (including the ones used in this paper, i.e., Lyman-break galaxies and LAEs). This approach is well within the reach of dedicated observations with ALMA—including recent ALMA Large Programs REBELS (PI: R. Bouwens) and the ALMA Lensing Cluster survey (PI: K. Kohno)—and will be complemented in the future with new systemic redshift measurements from the James Webb Space Telescope. Statistical approaches applied to existing ALMA data sets, such as the power spectrum analysis (as demonstrated in Uzgil et al. 2019 and Keating et al. 2020), provide efficient tools for probing low-fidelity emission from faint galaxies below survey detection thresholds. Data sets from line intensity mapping—tailored to this statistical approach—will also be available from ongoing and future experiments using instruments with a large field of view on single-dish telescopes (e.g., EoR-Spec (Cothard et al. 2020); SuperSpec (Redford et al. 2018; Karkare et al. 2020); CONCERTO (Lagache et al. 2018); TIME (Sun et al. 2020)) to probe aggregate [C II] emission at the highest redshifts.

The authors thank the anonymous referee for a constructive report. We thank Takuya Hashimoto for sharing equivalent-width data for the MUSE LAEs in ASPECS. B.D.U. would like to thank Andrea Ferrara and the cosmology group at Scuola Normale Superiore, where part of this work was done, for their hospitality and useful discussions. D.R. acknowledges support from the National Science Foundation under grant Nos. AST-1614213 and AST-1910107. D.R. also acknowledges support from the Alexander von Humboldt Foundation through a Humboldt Research Fellowship for Experienced Researchers. T.D.-S. acknowledges support from the CASSACA and CONICYT fund CAS-CONICYT Call 2018. H.I. acknowledges support from JSPS KAKENHI grant No. JP19K23462. ALMA is a partnership of ESO (representing its member

states), NSF (USA) and NINS (Japan), together with NRC (Canada), NSC and ASIAA (Taiwan), and KASI (Republic of Korea), in cooperation with the Republic of Chile. The Joint ALMA Observatory is operated by ESO, AUI/NRAO, and NAOJ.

Facilities: ALMA data: 2016.1.00324.L.

ORCID iDs

Pascal A. Oesch  <https://orcid.org/0000-0001-5851-6649>
 Fabian Walter  <https://orcid.org/0000-0003-4793-7880>
 Manuel Aravena  <https://orcid.org/0000-0002-6290-3198>
 Leindert Boogaard  <https://orcid.org/0000-0002-3952-8588>
 Chris Carilli  <https://orcid.org/0000-0001-6647-3861>
 Roberto Decarli  <https://orcid.org/0000-0002-2662-8803>
 Hanae Inami  <https://orcid.org/0000-0003-4268-0393>
 Rychard Bouwens  <https://orcid.org/0000-0002-4989-2471>
 Paulo C. Cortes  <https://orcid.org/0000-0002-3583-780X>
 Emmanuele Daddi  <https://orcid.org/0000-0002-3331-9590>
 Gergő Popping  <https://orcid.org/0000-0003-1151-4659>
 Dominik Riechers  <https://orcid.org/0000-0001-9585-1462>
 Mauro Stefanon  <https://orcid.org/0000-0001-7768-5309>
 Axel Weiss  <https://orcid.org/0000-0003-4678-3939>

References

- Aravena, M., Decarli, R., González-López, J., et al. 2019, *ApJ*, 882, 136
 Aravena, M., Decarli, R., Walter, F., et al. 2016, *ApJ*, 833, 71
 Bacon, R., Conseil, S., Mary, D., et al. 2017, *A&A*, 608, A1
 Bakx, T. J. L. C., Tamura, Y., Hashimoto, T., et al. 2020, *MNRAS*, 493, 4294
 Boogaard, L. A., Decarli, R., González-López, J., et al. 2019, *ApJ*, 882, 140
 Boogaard, L. A., van der Werf, P., Weiss, A., et al. 2020, *ApJ*, 902, 109
 Bouwens, R., González-López, J., Aravena, M., et al. 2020, *ApJ*, 902, 112
 Bouwens, R. J., Illingworth, G. D., Oesch, P. A., et al. 2010, *ApJL*, 709, L133
 Bouwens, R. J., Illingworth, G. D., Oesch, P. A., et al. 2015, *ApJ*, 803, 34
 Bradač, M., García-Appadoo, D., Huang, K.-H., et al. 2017, *ApJL*, 836, L2
 Brammer, G. B., van Dokkum, P. G., & Coppi, P. 2008, *ApJ*, 686, 1503
 Bruzual, G., & Charlot, S. 2003, *MNRAS*, 344, 1000
 Calzetti, D. 1997, *AJ*, 113, 162
 Capak, P. L., Carilli, C., Jones, G., et al. 2015, *Natur*, 522, 455
 Carilli, C. L., & Walter, F. 2013, *ARA&A*, 51, 105
 Carniani, S., Ferrara, A., Maiolino, R., et al. 2020, *MNRAS*, 499, 5136
 Carniani, S., Maiolino, R., Amorin, R., et al. 2018, *MNRAS*, 478, 1170
 Chabrier, G. 2003, *PASP*, 115, 763
 Cooke, E. A., Smail, I., Swinbank, A. M., et al. 2018, *ApJ*, 861, 100
 Cothard, N. F., Choi, S. K., Duell, C. J., et al. 2020, *JLTP*, 199, 898
 da Cunha, E., Groves, B., Walter, F., et al. 2013, *ApJ*, 766, 13
 Dayal, P., & Ferrara, A. 2018, *PhR*, 780, 1
 De Barros, S., Oesch, P. A., Labbé, I., et al. 2019, *MNRAS*, 489, 2355
 De Looze, I., Cormier, D., Lebouteiller, V., et al. 2014, *A&A*, 568, A62
 Decarli, R., Aravena, M., Boogaard, L., et al. 2020, *ApJ*, 902, 110
 Decarli, R., Walter, F., González-López, J., et al. 2019, *ApJ*, 882, 138
 Díaz-Santos, T., Armus, L., Charmandaris, V., et al. 2013, *ApJ*, 774, 68
 Díaz-Santos, T., Armus, L., Charmandaris, V., et al. 2017, *ApJ*, 846, 32
 Drake, A. B., Garel, T., Wisotzki, L., et al. 2017, *A&A*, 608, A6
 Dunlop, J. S., McLure, R. J., Biggs, A. D., et al. 2017, *MNRAS*, 466, 861
 Ellis, R. S., McLure, R. J., Dunlop, J. S., et al. 2013, *ApJL*, 763, L7
 Faisst, A. L., Fudamoto, Y., Oesch, P. A., et al. 2020, *MNRAS*, 498, 4192
 Ferrara, A., Vallini, L., Pallottini, A., et al. 2019, *MNRAS*, 489, 1
 Finkelstein, S. L., Ryan, R. E., Jr., Papovich, C., et al. 2015, *ApJ*, 810, 71
 Franco, M., Elbaz, D., Béthermin, M., et al. 2018, *A&A*, 620, A152
 Gehrels, N. 1986, *ApJ*, 303, 336
 González-López, J., Decarli, R., Pavesi, R., et al. 2019, *ApJ*, 882, 139
 González-López, J., Novak, M., Decarli, R., et al. 2020, *ApJ*, 897, 91
 Harikane, Y., Ouchi, M., Inoue, A. K., et al. 2020, *ApJ*, 896, 93
 Hashimoto, T., Inoue, A. K., Mawatari, K., et al. 2019, *PASJ*, 71, 71
 Hayatsu, N. H., Ivison, R. J., Andreani, P., et al. 2019, *RNAAS*, 3, 97
 Hayatsu, N. H., Matsuda, Y., Umehata, H., et al. 2017, *PASJ*, 69, 45
 Helou, G., Khan, I. R., Malek, L., & Boehmer, L. 1988, *ApJS*, 68, 151
 Hemmati, S., Yan, L., Díaz-Santos, T., et al. 2017, *ApJ*, 834, 36
 Herrera-Camus, R., Bolatto, A. D., Wolfire, M. G., et al. 2015, *ApJ*, 800, 1

- Illingworth, G. D., Magee, D., Oesch, P. A., et al. 2013, *ApJS*, **209**, 6
- Inami, H., Bacon, R., Brinchmann, J., et al. 2017, *A&A*, **608**, A2
- Inami, H., Decarli, R., Walter, F., et al. 2020, *ApJ*, **902**, 113
- Karkare, K. S., Barry, P. S., Bradford, C. M., et al. 2020, *JLTP*, **199**, 849
- Keating, G. K., Marrone, D. P., Bower, G. C., & Keenan, R. P. 2020, *ApJ*, **901**, 141
- Knudsen, K. K., Richard, J., Kneib, J.-P., et al. 2016, *MNRAS*, **462**, L6
- Kriek, M., van Dokkum, P. G., Labbé, I., et al. 2009, *ApJ*, **700**, 221
- Labbé, I., Oesch, P. A., Bouwens, R. J., et al. 2013, *ApJL*, **777**, L19
- Lagache, G., Cousin, M., & Chatzikos, M. 2018, *A&A*, **609**, A130
- Laporte, N., Katz, H., Ellis, R. S., et al. 2019, *MNRAS*, **487**, L81
- Le Fèvre, O., Béthermin, M., Faisst, A., et al. 2020, *A&A*, **643**, A1
- Loiacono, F., Decarli, R., Gruppioni, C., et al. 2021, *A&A*, **646**, A76
- Madau, P., & Dickinson, M. 2014, *ARA&A*, **52**, 415
- Mainali, R., Zitrin, A., Stark, D. P., et al. 2018, *MNRAS*, **479**, 1180
- Maiolino, R., Carniani, S., Fontana, A., et al. 2015, *MNRAS*, **452**, 54
- Matthee, J., Sobral, D., Boogaard, L. A., et al. 2019, *ApJ*, **881**, 124
- McLure, R. J., Dunlop, J. S., Cirasuolo, M., et al. 2010, *MNRAS*, **403**, 960
- Oesch, P. A., Bouwens, R. J., Illingworth, G. D., et al. 2010, *ApJL*, **709**, L16
- Oesch, P. A., Bouwens, R. J., Illingworth, G. D., et al. 2013, *ApJ*, **773**, 75
- Oesch, P. A., van Dokkum, P. G., Illingworth, G. D., et al. 2015, *ApJL*, **804**, L30
- Oke, J. B., & Gunn, J. E. 1983, *ApJ*, **266**, 713
- Pentericci, L., Carniani, S., Castellano, M., et al. 2016, *ApJL*, **829**, L11
- Pentericci, L., Vanzella, E., Fontana, A., et al. 2014, *ApJ*, **793**, 113
- Popping, G., Narayanan, D., Somerville, R. S., Faisst, A. L., & Krumholz, M. R. 2019, *MNRAS*, **482**, 4906
- Redford, J., Wheeler, J., Karkare, K., et al. 2018, *Proc. SPIE*, **10708**, 107081O
- Riechers, D. A., Pavesi, R., Sharon, C. E., et al. 2019, *ApJ*, **872**, 7
- Schaerer, D., Ginolfi, M., Béthermin, M., et al. 2020, *A&A*, **643**, A3
- Schenker, M. A., Stark, D. P., Ellis, R. S., et al. 2012, *ApJ*, **744**, 179
- Smit, R., Bouwens, R. J., Carniani, S., et al. 2018, *Natur*, **553**, 178
- Smit, R., Bouwens, R. J., Labbé, I., et al. 2016, *ApJ*, **833**, 254
- Stark, D. P., Richard, J., Charlot, S., et al. 2015, *MNRAS*, **450**, 1846
- Sun, G., Chang, T.-C., Uzgil, B. D., et al. 2020, arXiv:2012.09160
- Swinbank, A. M., Karim, A., Smail, I., et al. 2012, *MNRAS*, **427**, 1066
- Treu, T., Schmidt, K. B., Trenti, M., Bradley, L. D., & Stiavelli, M. 2013, *ApJL*, **775**, L29
- Uzgil, B. D., Carilli, C., Lidz, A., et al. 2019, *ApJ*, **887**, 37
- Vallini, L., Gallerani, S., Ferrara, A., & Baek, S. 2013, *MNRAS*, **433**, 1567
- Vallini, L., Gallerani, S., Ferrara, A., Pallottini, A., & Yue, B. 2015, *ApJ*, **813**, 36
- Verhamme, A., Garel, T., Ventou, E., et al. 2018, *MNRAS*, **478**, L60
- Walter, F., Decarli, R., Aravena, M., et al. 2016, *ApJ*, **833**, 67
- Whitaker, K. E., Ashas, M., Illingworth, G., et al. 2019, *ApJS*, **244**, 16
- Willott, C. J., Carilli, C. L., Wagg, J., & Wang, R. 2015, *ApJ*, **807**, 180
- Yamaguchi, Y., Kohno, K., Tamura, Y., et al. 2017, *ApJ*, **845**, 108
- Yan, L., Sajina, A., Loiacono, F., et al. 2020, *ApJ*, **905**, 147
- Zanella, A., Daddi, E., Magdis, G., et al. 2018, *MNRAS*, **481**, 1976
- Zitrin, A., Labbé, I., Belli, S., et al. 2015, *ApJL*, **810**, L12